PCCP

ROYAL SOCIETY OF CHEMISTRY

PAPER

View Article Online
View Journal | View Issue

Cite this: *Phys. Chem. Chem. Phys.*, 2025, **27**, 19762

The Kick Inside: time-resolved mechanistic insights into the DUV-driven interconversion of pyrazole to imidazole

Derri J. Hughes,[a] Wei Bo Ng,[a] Richard T. Chapman,[b] George Healing,[a] Michael A. Parkes,[c] Jennifer Rigden,[b] Oliver J. Smith,[b] Emma Springate,[b] James O. F. Thompson,[b] Tiffany Walmsley,[b] Joanne L. Woodhouse[a] and Russell S. Minns*[a]

The interconversion of aromatic heterocyclic molecules *via* photochemical scaffold-hopping provides a clean and efficient formation route to otherwise synthetically challenging targets. The interconversion between pyrazole and imidazole is a widely used example in materials science and biochemical applications with arrow-pushing mechanisms used to define the reaction path. To study the photochemically driven isomerisation of pyrazole to imidazole, we combine femtosecond time-resolved photoelectron spectroscopy experiments with *ab initio* electronic structure calculations. Our results show that excitation to the $^1\pi\pi^*$ state in the gas-phase provides a directed 'kick' to the system, resulting in the breaking of the N–N bond and formation of a ring-opened biradical intermediate on the vibrationally hot electronic ground state on ultrafast (sub-90 fs) timescales. Once on the vibrationally hot electronic ground state, production of the imidazole photoproduct proceeds *via* the formation of a three membered ring that subsequently opens and shifts the relative position of the two nitrogen atoms.

Received 14th July 2025,
Accepted 23rd August 2025

DOI: 10.1039/d5cp02684a

rsc.li/pccp

1 Introduction

Aromatic heterocyclic molecules—organic ring systems containing one or more non-carbon atoms and a delocalised electron cloud—play essential roles across a wide range of biological systems. They function as central chromophores for ultraviolet (UV) absorption in photoactive processes and serve as key structural subunits in many bioactive compounds.[1–4] These molecules also play a major role in synthetic photochemistry due to their inherent stability and versatility, providing access to natural products and molecular scaffolds in milder conditions that are otherwise challenging to obtain through traditional synthetic methods.[5–8] As a result, there is a renewed interest in understanding how UV-induced changes in electronic structure can drive novel and selective scaffold-hopping reactions.[9–12] A particularly notable example, which serves as the focus of this work, is the photochemical interconversion of pyrazole and imidazole—two core aromatic heterocyclic isomers prevalent in small molecule drug target design[13] and organic electronic materials.[14,15]

As with all photochemical transformations, the geometric structural changes that occur during this interconversion process are driven by the changes in electronic structure and reactivity on the excited state. However, despite pyrazole's wide use and importance, it remains unclear what electronic state changes occur, and how important these are in directing the interconversion between scaffold structures. Herein, we present the results of extreme ultraviolet (XUV) time-resolved photoelectron spectroscopy (TRPES) measurements that monitor the initial excited state dynamics, formation of vibrationally hot ground state pyrazole, and its isomerisation to imidazole. These experimental observations are expanded upon through the use of high-level *ab initio* electronic structure calculations which map the dominant isomerisation pathway, identifying the key intermediates and structural dynamics involved.

Within the organic chemistry literature, two curly arrow mechanisms that have been used to define the pyrazole to imidazole reaction path are illustrated in Fig. 1.[12] The first, coined the biradical pathway, involves N–N bond fission, generating a biradical intermediate, **1a**, that transitions through a strained three-membered ring, **1b**, before forming imidazole. The second, known as the bicyclic pathway, begins with out-of-plane ring distortions, producing bicyclic intermediates, **2a** and

[a] *School of Chemistry and Chemical Engineering, University of Southampton, University Road, Highfield, Southampton, SO17 1BJ, UK. E-mail: R.S.Minns@soton.ac.uk*
[b] *Central Laser Facility, STFC Rutherford Appleton Laboratory, Didcot, Oxfordshire OX11 0QX, UK*
[c] *Department of Chemistry, University College London, 20 Gordon Street, London, WC1H 0AJ, UK*

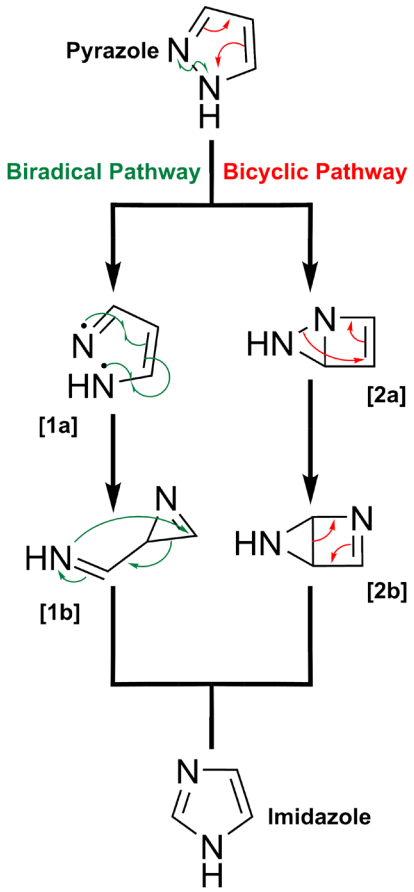

Fig. 1 Proposed curly arrow mechanisms for both the bicyclic (red) and biradical (green) pathways of photoisomerisation of pyrazole to imidazole.[12]

2b, *en route* to imidazole formation. The role of the electronically excited states involved and the route back to the electronic ground state are, however, ill-defined in such mechanisms.

Previous theoretical studies have utilised complete active space self-consistent field (CASSCF) calculations to examine the geometries of the conical intersections (CIs) involved in the two proposed pathways.[16,17] Three types of CIs were identified and classified according to their associated pathway: N–H dissociation, N–N bond stretching leading to the biradical intermediate, and ring puckering leading to the bicyclic intermediate. These biradical and bicyclic geometries align with those depicted in the proposed curly arrow mechanisms (Fig. 1). Additional trajectory-based simulations of the dynamics suggest that the excited state has a lifetime of only 150 fs, suggesting that the main structural changes predominantly occur on a vibrationally hot ground state, mediated by one, or several, CIs.[17]

Experimental measurements of the UV-driven dynamics of pyrazole (and its structural analogue imidazole) in the gas phase have, to date, been focused on pathways orthogonal to the photoisomerisation, chiefly that of N–H photolysis.[5–8,18,19] Previous experiments have utilised frequency- and time-resolved velocity map imaging (VMI) and ion yield (IY) techniques to investigate the H-atom photodissociation dynamics of pyrazole after excitation at pump wavelengths between 200–220 nm.[6,18,19] Time-resolved VMI studies reported the appearance of high kinetic energy H-atoms on a sub-50 fs timescale,[6,18] which, in agreement with previous frequency-resolved VMI studies,[19] was assigned to a direct dissociation process occurring following excitation on to the $^1\pi\sigma^*_{NH}$ state. Secondary, much weaker, peaks associated with $C_2H_3N^+$, $C_2H_2N^+$, CH_2N^+, and CH_2^+ products were also observed in the time-resolved IY measurements of Williams *et al.* The formation of these fragments was assigned to ionisation processes occurring after excitation of a $^1\pi\pi^*$ state and subsequent relaxation through a ring-puckered $^1\pi\pi^*/S_0$ conical intersection.[18] The observation of these fragments suggests alternative ring fragmentation/ring deformation pathways that could lead to the eventual formation of imidazole but provide little mechanistic detail of how this might proceed.

The experimental and computational insights into pyrazoles photochemistry to date therefore provide a rather disconnected picture, with experiments predominantly focussed on the H-atom photodissociation pathway and theory identifying conical intersection pathways that lead back to the electronic ground state. The overall mechanism of the pyrazole-imidazole photoisomerisation reaction therefore remains untested and unclear. This work aims to provide clarity on the driving photoisomerisation mechanism.

2 Methodologies

2.1 Experimental

Time-resolved photoelectron spectroscopy measurements were performed using the atomic, molecular and optical (AMO) endstation at Artemis at the Central Laser Facility. An in-depth experimental setup is given elsewhere[20] with only a brief overview given below.

Pump and probe pulses were generated from the output of an amplified Ti:Sapphire system (Red Dragon, KM Labs), operating at a central wavelength of 800 nm at a 1 kHz repetition rate. The output was split providing separately compressed pulses that were used to generate the pump and probe. A 200 nm pump was generated using a BBO-based fourth harmonic generation setup. This featured an initial frequency doubling stage (800 nm → 400 nm), followed by two serial sum frequency stages (800 nm + 400 nm → 266 nm; 266 nm + 800 nm → 200 nm). This produced 5 μJ of 200 nm light which was reduced down by an aperture to provide approximately 2.5 μJ per pulse on the target. XUV probe pulses were generated *via* high harmonic generation (HHG) in an Ar gas jet. The HHG process was driven by the second harmonic (400 nm) of the 800 nm fundamental, with a quasi-time-preserving monochromator used to select the 7th harmonic of the 400 nm driver (21.6 eV, 57.4 nm). The isolated harmonic had a nominal flux of 10^{10} photons per second on target.[21] Both pump and probe pulses were linearly polarised parallel to the TOF axis

(perpendicular to the detector plate), independently propagated, focused, and overlapped at a small crossing angle ($\sim 3^\circ$) at the interaction point with the electron time-of-flight spectrometer and the effusive molecular beam. The resulting pump–probe cross-correlation, obtained from our fitted instrument response function, yielded a Gaussian pulse duration (σ) of 83 $\pm$ 6 fs.

A continuous effusive molecular beam was generated by gently heating solid pyrazole (Sigma Aldrich) to 55 °C. The resultant vapour was expanded through a nozzle of diameter 3 mm positioned 30 mm from the interaction point with the flow rate controlled by a low rate leak valve (Chell CMV-VFM-2-P-44). Liberated photoelectrons were detected using an electron time-of-flight spectrometer (Kaesdorf ETF11) with a collection efficiency of 5%, and an entrance lens voltage optimised for photoelectrons with kinetic energies associated with the initial excited states and vibrationally hot ground state (15–19 eV, approx. 95 V). Pump–probe data was collected over 26 delays, ranging from −1 to +100 ps with a total of approximately 3.86 $\times$ 10^6 laser shots recorded per delay point.

2.2 Theory

Potential energy curves (PECs) of pyrazole were obtained using state-averaged complete active space self-consistent field (SA-CASSCF) calculations. Multi-state complete active space and second-order perturbation theory (XMS-CASPT2) corrections on the ground (S_0) and first excited states (S_1) were applied as single point calculations providing a balance between computational cost and accuracy in comparison to full XMS-CASPT2 geometry optimisations. All excited state calculations employed the aug-cc-pVDZ basis set. The initial ground state geometry was optimised using density functional theory (DFT) with the B3LYP functional[22–24] in the ORCA 6.0.0 package[25] which was used to generate the natural bond orbitals and construct the active space. The active space of 12 electrons in 10 orbitals, presented in Fig. 2, consists of two pairs of π and π^* orbitals, the p_z orbital of N1, the *n* orbital of N2, a pair of N1–N2 σ and σ^* orbitals and a pair of N1–C5 σ and σ^* orbitals. We also define the highest occupied and lowest unoccupied molecular orbitals (HOMO and LUMO) of the active space. The orbitals are chosen so as to encompass those required in both the bicyclic and biradical isomerisation pathways. Subsequently, the S_0 and S_1 states were optimised at the SA-CASSCF(12,10) level, and relaxed surface scans were conducted from these geometries using ORCA 6.0.0. Further XMS-CASPT2(12,10) corrections were applied in the BAGEL 1.2 package[26] using the SS-SR contraction scheme, cc-pVDZ-jkfit basis for density fitting and a 0.1 a.u. imaginary shift to remove influence from intruder states. All minima and transition states were characterised through numerical frequency calculations. All geometries were visualised with the VMD software.[27] For the N1–H dissociation pathway, we expand the active space to also include σ_{NH} and σ^*_{NH} orbitals and calculated the cut along the N–H stretching coordinate at a XMS-CASPT2 corrected SA-CASSCF(14,12)/aug-cc-pVDZ level of theory.

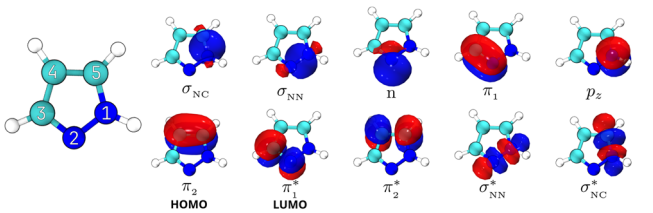

Fig. 2 Natural bonding orbitals of pyrazole making up the active space used in XMS-CASPT2(12,10) corrected SA-CASSCF(12,10)/aug-cc-pVDZ calculations. In this and all subsequent figures, nitrogen atoms are displayed in dark blue, carbon atoms in light blue, and hydrogen atoms in white. Numbers on each atom are used to define positions in the initial pyrazole ring. This includes two pairs of π and π^* orbitals, the n orbital of N2, the p_z orbital of N1 and a pair of σ and σ^* orbitals of the N1–C5 and N1–N2 bonds. HOMO is the highest occupied molecular orbital whereas LUMO is the lowest unoccupied molecular orbital.

The computed XMS-CASPT2(12, 10) $S_1 \leftarrow S_0$ vertical excitation energy is 6.22 eV. For comparison, the uncorrected SA-CASSCF(12,10) method yields a value of 6.49 eV, while TD-B3LYP gives 5.8 eV. Although TD-B3LYP produces vertical excitation energies that are consistent with experimental values,[28] its single-reference framework limits its ability to accurately describe multiconfigurational excited state dynamics. The XMS-CASPT2 corrected vertical excitation energy (6.22 eV) overestimates the experimentally reported vertical transition energy (5.8 eV).[28] We therefore treat this $\sim$0.4 eV deviation as a reasonable upper bound on the uncertainty in our computed excitation energies, which remain appropriate for modelling the reaction pathways initiated under our experimental conditions.

After mapping the excited state pathways of pyrazole, potential reaction pathways on the ground state are calculated using the climbing image nudged elastic band (NEB) method[29] at the DFT/B3LYP level, as implemented in the ORCA 6.0.0 package. Given the computational expense associated with NEB calculations, our choice of using the B3LYP functional was based on its use in other investigations of photochemically-driven ground state reaction dynamics,[30–32] and ultimately provides a reasonable balance between feasibility and accuracy. The number of intermediate images was set to 20, and the initial trajectory was generated using the sequential image dependent pair potential (SIDPP) method. Then, the path was refined at the semi-empirical GFN2-xTB level of theory[33] before being further refined at the B3LYP level of theory. Optimised ground state equilibrium geometries of pyrazole and imidazole obtained using the B3LYP functional served as the starting and final images of the reaction pathway. For the NEB calculation, the corresponding S_1/S_0 CI, optimised at the SA-CASSCF(12,10)/aug-cc-pVDZ level of theory, was utilised as a guess transition state. To ensure accurate evaluation of integrals, all DFT calculations utilised the defgrid3 option for finer grid spacing.

3 Results and discussion

3.1 Experimental results

In Fig. 3, an overview of the data collected and the resultant fits are plotted. In (a), the background subtracted time-resolved photoelectron spectrum collected over a pump–probe delay

time range of −0.6 to +2.5 ps is presented. At time-zero (grey dashed line), we observe a short-lived excited state feature that is initially observed at a binding energy close to 3.5 eV, which shifts to higher binding energies at later times. Given the 9.3 eV binding energy of ground state pyrazole and the 5.8 eV excitation energy associated with the $S_1 \leftarrow S_0$ transition, the excited state signal would be expected at an initial binding energy of 3.5 eV.[28] Therefore, we assign the signal at 3.5 eV to the S_1 excited state. As the S_1 excited state population decays, a long-lived signal in the 7.5–8.6 eV region is observed. The longer-lived feature in Fig. 3a appears to be relatively featureless and is consistent with that of a vibrationally hot ground state – such signals are typically associated with a mixture of differing geometric structures.[34] By averaging the photoelectron spectrum over selected delay time ranges across the full 100 ps window (Fig. 3b), we observe a broad continuous band between 7.5 and 8.6 eV, which we assign to a vibrationally hot ground state. In addition, a feature centred at 8.8 eV aligns with the expected ionisation potential of imidazole.[35] Although this peak appears well defined in the difference spectrum, its true width is likely broader; overlap with depletion of the pyrazole ground state signal makes an accurate lineshape difficult to extract. To assess its temporal evolution, Fig. S2 shows the time-dependent intensity profile of the 8.65–8.85 eV binding energy region as a function of delay time. Although the profile is notably noisy and does not reveal any distinct temporal structure that would allow for a clear assignment, a comparison of the centre of mass delay point intensities before and after time zero (further details in the SI) suggests a gradual increase, with higher intensities appearing on a ∼17–20 ps timescale. Therefore, while the peak at 8.8 eV strongly suggests that imidazole is formed, we do not rule out the possibility that

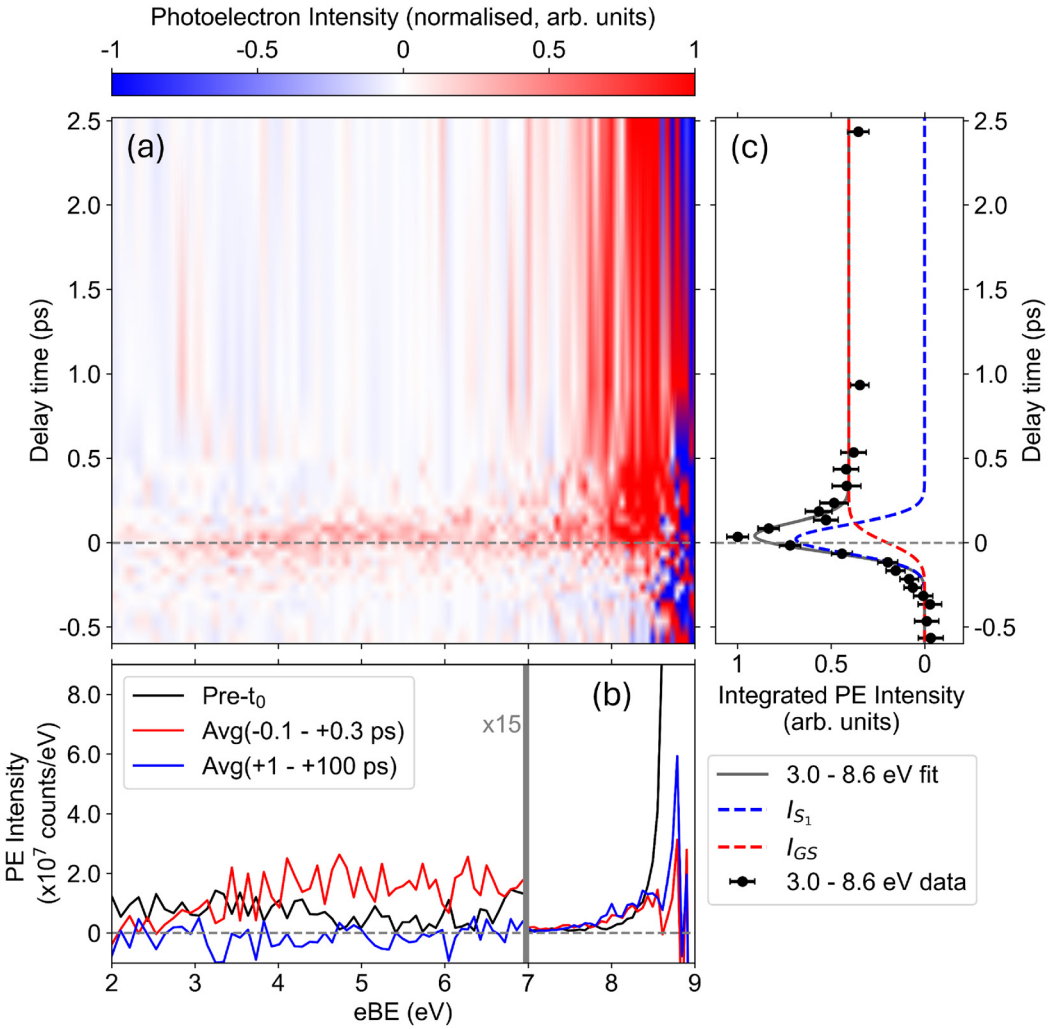

Fig. 3 (a) Background subtracted time-resolved photoelectron spectrum over the −0.6 to +2.5 ps pump–probe delay range. The grey dashed line denotes the fitted time-zero (+66 fs). (b) Time-averaged (Avg) background subtracted spectra over the −0.1 to +0.3 ps (red), and +1 to +100 ps (blue) delay ranges alongside the pre-time-zero background (black). Photoelectron (PE) intensities within the 2–7 eV range have been multiplied by a factor of 15 for clarity. (c) Integrated intensity of the time-resolved signal over the 3–8.6 eV energy range (black dots) is plotted as a function of delay time. The kinetic fits described in the main text are plotted as grey, red and blue dashed lines. 95% confidence intervals (error bars) obtained by case resampling bootstrap analysis of the data (see SI for further details) are also plotted.

this signal could also be an extension of vibrationally hot ground state structures.

To extract timescales associated with the decay of the electronically excited state signal, a kinetic model was fit to the integrated intensity over the 3.0–8.6 eV region of the photoelectron spectrum. The full energy range is covered due to the relatively weak and continuous binding energy signal that makes integration over smaller, more discrete regions of the spectrum challenging. As the initial S_1 population (eBE: 3.5–7.5 eV, I_{S_1}) decays into a vibrationally hot ground state (eBE: 7.5–8.6 eV, I_{GS}), we can model the total signal intensity (I) as

$$I = I_{GS} + I_{S_1}, \quad (1)$$

where I_{GS} describes the rise in the vibrationally hot ground state signals, and I_{S_1} describes the S_1 state signals. I_{S_1} is described as the Gaussian instrument response function convoluted with an exponential decay function:

$$I_{S_1} = Ae^{-\lambda_{S_1}(t-t_0)}e^{\frac{(\sigma\lambda_{S_1})^2}{2}}\left(1+\mathrm{erf}\left(\frac{t-t_0-\sigma^2\lambda_{S_1}}{\sqrt{2}\sigma}\right)\right), \quad (2)$$

where A is the fitted amplitude, λ_{S_1} is the fitted decay constant associated with the population of the S_1 state, σ is defined by the Gaussian instrument response, and t_0 is time-zero. Due to its apparent long-lived nature, I_{GS} can be described as a step function, which rises as the population in the S_1 state decays:

$$I_{GS} = B\left(\left(1+\mathrm{erf}\left(\frac{t-t_0}{\sqrt{2}\sigma}\right)\right) - I_{S_1}\right), \quad (3)$$

where B is the fitted amplitude of the step function. All other parameters have been defined and are extracted from eqn (2). Both values for A and B account for differences in ionisation cross sections and detection within their respective integrated binding energy regions. The resultant fit to the integrated data and its individual fitted components (I_{S_1} and I_{GS}) are presented in Fig. 3c alongside their 95% confidence intervals (error bars) obtained from case resampled bootstrap analysis of the data (see SI for further details). The extracted timescale associated with the decay of the S_1 state is 23 ± 5 fs. As this is almost four times smaller than our instrument's temporal resolution (σ) of 83 ± 6 fs, this 23 fs time constant is taken as indication of an ultrafast process rather than a precise quantitative measurement of the excited state lifetime.

The experimental data therefore points to a rapid relaxation pathway leading back to a vibrationally hot ground state on a sub-90 fs timescale where it appears most of the nuclear rearrangements associated with the isomerisation to imidazole will occur. To explore this process in more detail, a series of theoretical calculations have been performed.

3.2 Excited state pathways

The equilibrium geometries of the S_0 and S_1 surfaces (Fig. 4) and cuts along specific reaction coordinates (Fig. 5) have been calculated according to the methods outlined in Section 2.2. The optimised structures of S_0 and S_1, Fig. 4, reveal that upon excitation, the N1–N2, N2–C3, C3–C4, C4–C5, and C5–N1 bonds

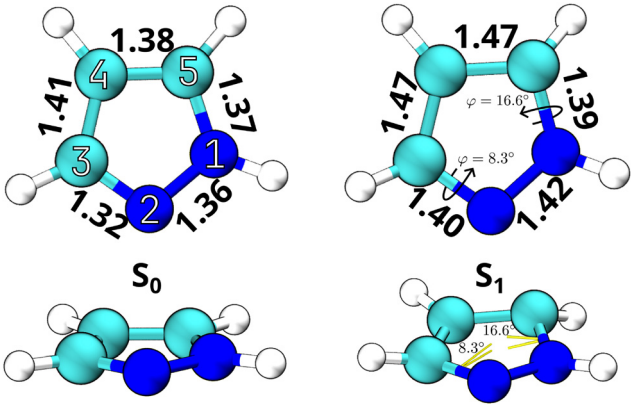

Fig. 4 SA-CASSCF(12,10)/aug-cc-pVDZ optimised geometries of pyrazole in the S_0 and S_1 states. Bond lengths are given in Angstroms.

in the ring are elongated by 0.06, 0.08, 0.06, 0.09, and 0.02 Å respectively, indicating the ππ* character of the excitation. Additional out of plane torsions around the dihedrals (φ) $\varphi_{N2-N1-C5-C4}$ and $\varphi_{N1-N2-C3-C4}$ lead to angles of 16.6° and 8.3° respectively in the S_1 equilibrium geometry. Confirmation of these state minimum structures was given by the absence of imaginary frequencies (see SI).

The two equilibrium structures suggest that, upon excitation, there will be ring expansion and out of plane deformations on the S_1 surface, indicating the forces acting on the molecule could lead to either bicyclic or biradical intermediates. Previous calculations have suggested that there are multiple S_1/S_0 CIs along both the biradical (N1–N2 fission) and bicyclic pathways which lead back to the electronic ground state.[16,17] To explore the locations of the CIs and their relevance in the overall isomerisation dynamics, relaxed scans of the S_1 potential energy surface were performed along the N1–N2 and N1–H bond stretch coordinates, as well as the $\varphi_{N2-N1-C5-C4}$ and $\varphi_{N1-N2-C3-C4}$ dihedral angle coordinates. We present the 1D PECs in Fig. 5a–d respectively, with the S_0 PEC calculated at the same geometries.

In Fig. 5a, on the S_1 surface, a shallow minimum is observed at an N1–N2 distance of 1.42 Å, corresponding to the geometry depicted in Fig. 4. Analysis of the LUMO at this bond length, plotted above the PEC, confirms a strong ππ* electronic character (plotted in blue) for the state. As the bond is further extended, the curve transitions almost barrierlessly into a strongly repulsive region, culminating in an S_1/S_0 CI at approximately 2.5 Å. At a bond length of 1.6 Å, the π* LUMO appears to mix with the σ^*_{NN} orbital, which then evolves into a localised σ^*_{NN} orbital by 1.75 Å. The electronic character of the S_1 state becomes predominantly πσ* (plotted in green), which mediates further extension of the N1–N2 bond and provides access to the S_1/S_0 CI. While this state crossing point has not been explicitly optimised, analysis of the evolution of the LUMO in the active space with increasing N1–N2 distance confirms the crossing through reordering and mixing of the σ^*_{NN} and π^* orbitals.

As the N1–H bond stretches, in Fig. 5b, the S_1 curve exhibits a significant energy barrier of approximately 0.5 eV that any

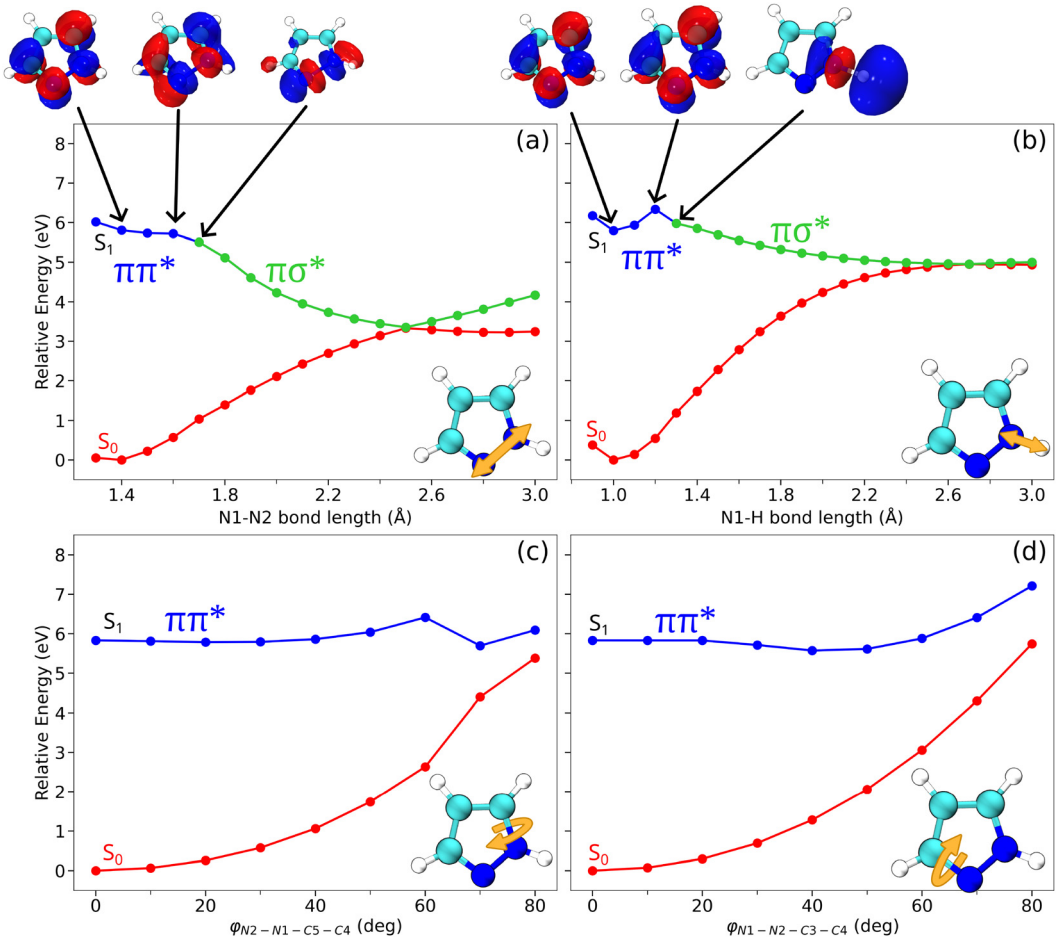

Fig. 5 Relaxed scans along the (a) N1–N2 and (b) N1–H bond stretching coordinates, and (c) $\varphi_{N2-N1-C5-C4}$, and (d) $\varphi_{N1-N2-C3-C4}$ dihedral angles on the S_0 and S_1 electronic states of pyrazole. Calculations of (a), (c) and (d) were performed at the XMS-CASPT2(12,10) corrected SA-CASSCF(12,10)/aug-cc-pVDZ level of theory. (b) was conducted at an expanded active space, including both N–H σ and σ* molecular orbitals alongside corresponding XMS-CASPT2 single point corrections. The evolution of the lowest occupied molecular orbital (LUMO) at various geometries is shown above, for the N1–N2 and N1–H relaxed scans.

excited state population must overcome to undergo N–H dissociation. This barrier peaks at a bond length of 1.2 Å. After this point, the curve becomes repulsive, coinciding with a change in the electronic character of the excited state to $\pi\sigma^*_{NH}$ (plotted in green). This change indicates a crossing point between two electronic states. Such a crossing is expected and has been previously reported in studies of N–H photodissociation in pyrazole.[6,18,19] We plot the evolution of the LUMO as the N1–H bond extends above the PEC. In addition, an S_1/S_0 CI is observed at a bond length of approximately 2.6 Å on the asymptotic limit of both S_1 and S_0 states. At this point, the two fragments no longer interact with each other. Due to its location, this CI is not expected to play a major role in ground state recovery and the overall photoisomerisation dynamics. Instead, it may act as a competing channel for any excited state population. Previous computational work at the MS-CASPT2 level reported the conical intersection (CI) location at approximately 2.1 Å, with dissociation channels leading to both $C_3H_3N_2$ (X) and $C_3H_3N_2$ (A) products.[6,17,19] While the CI computed in this work is shifted to 2.6 Å, with the two dissociation channels occurring at longer N1–H bond lengths, we can still rule out this pathway as a significant contributor to photoisomerisation for the same reasons discussed above. We also plot the uncorrected SA-CASSCF(14,12) PECs in Fig. S4 (see SI), which successfully reproduces the previously reported N1–H PECs.

In Fig. 5c and d, the S_1 state surfaces remain relatively flat as their respective dihedral angle increases until 50°. No CIs are observed along these coordinates with limited indication of any force directing the molecules away from relatively planar geometries. We note, however, surfaces constructed by linear interpolations of internal coordinates computed by Xie and Su obtained an S_1/S_0 CI along the $\varphi_{N2-N1-C5-C4}$ and $\varphi_{N1-N2-C3-C4}$ axes at 55° and 60° respectively, suggesting that multidimensional changes give rise to the degeneracy between states which are not captured by constrained surface scans.[16,17] As an alternative to the minimum energy reaction paths computed in Fig. 5, we performed CI optimisations on both the $\varphi_{N2-N1-C5-C4}$ and $\varphi_{N1-N2-C3-C4}$ S_1 state surfaces at the SA-CASSCF(12,10)/aug-cc-pVDZ level. Between the S_1 optimised minimum energy

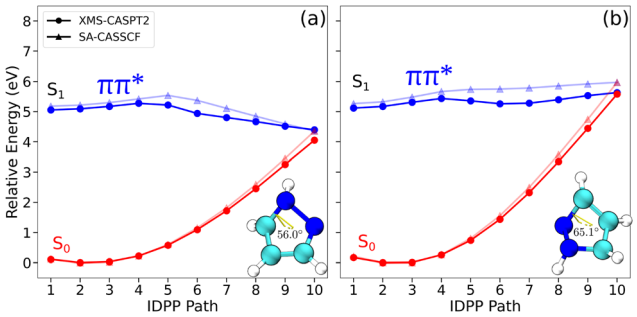

Fig. 6 Image-dependent pair potential excited state pathways for both $\varphi_{N2-N1-C5-C4}$ (a) and $\varphi_{N1-N2-C3-C4}$ (b) from the S_1 minimum geometry to the optimised S_1/S_0 CI as a function of the reaction coordinates (IDPP Path). The ball and stick structures shown are the respective optimised CI geometries. Both pathways were calculated at the SA-CASSCF(12,10)/aug-cc-pVDZ level of theory (triangles). XMS-CASPT2(12,10) corrected pathways are overlaid (circles).

geometry and the optimised CI geometries, we generated a series of image-dependent pair potential (IDPP) structures and formed representative excited state pathways to the CIs which are plotted in Fig. 6. We note that these geometries represent unoptimised structures in which any energy barrier is regarded as the upper bound of the actual energy barrier and is thus not representative of a minimum energy reaction path.

In the IDPP pathways, we find S_1/S_0 CIs at $\varphi_{N2-N1-C5-C4} = 56^\circ$ (Fig. 6a) and at $\varphi_{N1-N2-C3-C4} = 65^\circ$ (Fig. 6b) respectively, while preserving a $\pi\pi^*$ electronic character of the excited state. These extracted CI dihedral angles are in agreement with those obtained by Xie[17] and Su.[16] Although these are not present in the minimum energy paths presented in Fig. 5c and d, we note that there are key differences in the CI geometries. The optimised CI geometries are presented in Fig. S6 and S7 (see SI). Briefly, the main differences in these geometries include H-atom pointing (both), C2–N4 bond length (Fig. 6a), and ring puckering (Fig. 6b). We note that the optimised CI structures closely resemble the bicyclic structures proposed in Fig. 1. In Fig. 6, we also overlay the XMS-CASPT2 corrected IDPP pathways which, in the case of (b), agree with the position of the CI. In (a) however, the XMS-CASPT2 correction appears to lift the degeneracy between states suggesting that the SA-CASSCF optimised CI is not sufficiently accurate. Regardless of this point, and in common with the previous works of Xie[17] and Su,[16] routes to both dihedral CIs from the S_1 minimum are energetically flat, with no apparent directional gradient driving the system towards the state crossings.

Our excited state pathways strongly suggest that ground state recovery is mediated by the fission of the N1–N2 bond. Our ultrafast experimental lifetime of the S_1 state suggests that the changes in nuclear geometry on the excited state are fast, highly directed, and most likely along a well-defined, single reaction coordinate. Based on their flat potentials and no apparent driving force to funnel the excited state population into the S_1/S_0 CI on the experimentally-derived timescale, the IDPP paths connecting the S_1 minimum and optimised dihedral CI structures can be ruled out as a viable path to mediate isomerisation *via* ground state recovery. We rule out the involvement of the N1–H minimum energy pathway in the recovery of the ground state due to the barrier on the S_1 surface. Therefore, we are left with one viable pathway that can mediate ground state recovery in the isomerisation mechanism: N1–N2 bond fission, forming a biradical intermediate *en route*, on the ultrafast timescale measured in the experiment.

3.3 Structural dynamics on the ground state

To characterise the isomerisation dynamics of the system upon traversing the N1–N2 S_1/S_0 CI and reaching the electronic ground state, we calculate the reaction pathway leading to the imidazole product at the DFT/B3LYP level using the NEB method. Starting from the S_1/S_0 CI, we find further structural rearrangement pushes the system to a local minimum through C3–N2–C4 cyclisation, forming a three membered ring. This closely resembles structure **2a** in Fig. 1 and is labelled as Minimum in Fig. 7. At this point, we estimate that the system will have excess energy of ~4 eV (pump energy – Minimum energy). This excess energy is likely to be converted into vibrational energy due to the lack of a heat sink in the gas-phase to dissipate this excess energy. Our reaction pathway shows that this energy is applied across the C3–C4 bond resulting in bond cleavage (C–C bond enthalpy: 3.6 eV[36]) thus forming the transition state structure (TS) shown in Fig. 7. Once the N2 atom is brought into the chain, bond formation between C3 and N1 occurs, yielding imidazole. Numerical calculation of the Hessian confirms the presence of one imaginary frequency at the TS. Additionally, an intrinsic reaction coordinate calculation links the local minimum to imidazole *via* the TS. We present these further calculations in Fig. S8 (see SI).

3.4 Discussion

Based on the combined experimental and theoretical results, a compelling unified picture of the photoisomerisation process is

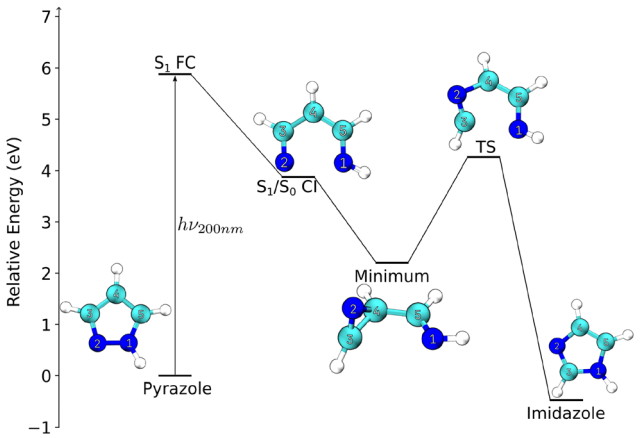

Fig. 7 Schematic reaction profile for the pyrazole-imidazole isomerisation based on the combined excited state and ground state NEB calculations. Energies of the critical geometries have been calculated at the B3LYP/aug-cc-pVDZ level and are scaled relative to pyrazole. S_1 FC relates to the Franck–Condon geometry formed upon excitation to the S_1 state.

Table 1 Comparison of experimental and calculated binding energies for the critical structures shown in Fig. 7. Experimental values are taken from ref. 35 and this work. Theoretical values were obtained at the B3LYP/aug-cc-pVDZ level, except for the pyrazole S_1 minimum, which was computed using CASSCF(12,10)/aug-cc-pVDZ

Structure	Pyrazole	Pyrazole S_1 minimum	CI	Minimum	TS	Imidazole
	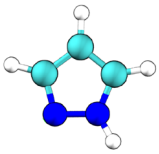	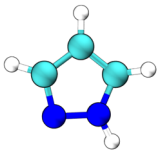	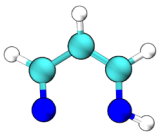	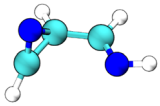	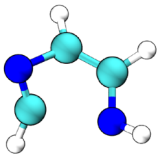	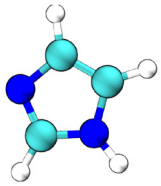
Experimental (eV)	9.15	3.50	—	—	—	8.78
Theoretical (eV)	9.35	3.72	8.31	9.81	7.84	8.86

given in Fig. 7 and can be summarised as follows. Upon excitation by 200 nm, pyrazole is excited into the S_1 state that at the Franck–Condon geometry if of $^1\pi\pi^*$ character. As the N1–N2 bond stretches, the character of the adiabatic S_1 state gains $\pi\sigma^*_{NH}$ character, and follows a repulsive potential along the N1–N2 bond stretching dimension towards an S_1/S_0 CI located at an N1–N2 separation of 2.5 Å. Our experimental observations place an upper limit on the time-scale for this process, with population of the ground state occurring in less than 90 fs. After passage through the CI, the wavepacket can follow one of two pathways on the electronic ground state where the molecule will either reform pyrazole through restoration of the N1–N2 bond (Fig. 5a), or evolves towards a local minimum energy structure associated with the formation of a three-membered, C3–N2–C4, ring (Fig. 7). Subsequent structural changes lead to the formation of imidazole by first breaking the C3–C4 bond and forming a new bond between the N1–C3 atoms to form the ring-closed imidazole structure.

Despite being applied to distinct regions of the reaction landscape—CASSCF/XMS-CASPT2 for excited state pathways and CIs, and DFT for ground state NEB calculations—the two methods yield a coherent mechanistic picture that overwhelmingly supports the previously proposed biradical isomerisation pathway in Fig. 1 and validates their complementary use.

To check consistency with the experimental observations, binding energies for the critical geometries involved in the reaction have been calculated at the B3LYP/aug-cc-pVDZ level of theory in accordance with Koopman's theory. We tabulate these values in Table 1 alongside experimental values where available. Comparing these values to the spectra plotted in Fig. 3a and b, we see peaks at long delays around the 8.8 eV value expected for the imidazole product. Ionisation energies for the other structures identified as reaction intermediates fall within the experimentally observed broad energy range (Fig. 3b), indicating that within the gas-phase ensemble measured, we have a distribution of these vibrationally hot ground state structures. From our kinetic fits in Fig. 3c of the 7.5–8.6 eV region, we expect these structures to be accessed on a sub-picosecond timescale. Based on these calculations, we tentatively assign the peak at 8.8 eV in Fig. 3b to imidazole.

Previous experiments have observed H-atom photodissociation dynamics. To determine the spectral signature of this process, we calculated the binding energy of the pyrazolyl radical ($C_3H_3N_2$) which would be formed as a co-fragment. The binding energy was determined to be 10.6 eV (B3LYP/aug-cc-pVDZ), overlapping with ground state background signals (see Fig. S1). This overlap complicates the isolation of this signal as the corresponding region of the photoelectron spectrum is largely dominated by ionisation from ground state pyrazole. However, given the barrier to N–H bond dissociation from the $^1\pi\pi^*$ state, and the ultrafast relaxation observed we suggest that any N–H dissociation from the channel is minor. This agrees with previous measurements of the N–H photolysis reaction performed at similar wavelengths that suggest the N–H photolysis occurs following excitation into a close lying $^1\pi\sigma^*$ states.[6,18,19] Importantly, these studies have employed detection techniques that are uniquely sensitive to the dissociating H atom. Our measurements do not provide any direct observation of this pathway, suggesting that the fragments produced by this channel are below our limit of detection. To rationalise this finding, we calculated the oscillator strengths of both the $^1\pi\pi^*$ and $^1\pi\sigma^*$ states at the TD-B3LYP/aug-cc-pVDZ level of theory. Although both states are energetically accessible in our pumping regime ($^1\pi\sigma^*$ = 6.1 eV; $^1\pi\pi^*$ = 5.8 eV), the oscillator strength of the $^1\pi\pi^*$ transition (6.54×10^{-3}) is over two orders of magnitude greater than that of the $^1\pi\sigma^*$ transition (4.26×10^{-5}). This large disparity suggests that direct excitation to the dissociative $^1\pi\sigma^*$ state is much less probable, consistent with the absence of experimental evidence for this channel in our measurements.

4. Conclusions

Using a combination of advanced experimental and theoretical methods, the photoisomerisation dynamics of the pyrazole to imidazole after excitation by 200 nm have been studied. XUV-TRPES measurements have been coupled with *ab initio* electronic structure calculations of the S_0 and S_1 states. Our combined efforts suggest that the photoisomerisation of pyrazole in the gas-phase proceeds through a biradical pathway with little-to-no competition with the bicyclic pathway. The experimental observations suggest that, while this is a photochemically-driven process, the electronic excitation is extremely short-

lived and effectively acts as a directed "*kick*" for the system to overcome the barrier to N1–N2 dissociation. The majority of the dynamics occur in the electronic ground state where photoelectron signals associated with the range of structures that could be formed are strongly overlapped.

Recently performed ultrafast electron diffraction experiments will provide a further test of the conclusions here, allowing us to directly identify key intermediate structures. Combining such structural probes with the electronic state sensitivity of photoelectron spectroscopy and advanced theoretical modelling will provide a unified picture of the coupled electronic and geometric structure changes involved here and in other important photochemical systems.

While these results show that the biradical pathway is the dominant isomerisation pathway in the gas-phase, they may not necessarily reflect the dynamics that occur in solution where the dominant pathway may be mediated by bicyclic intermediates, or by the destabilisation of the biradical intermediate by solvent effects which would change the electronic character of the excited state. Further transient vibrational absorption studies should be conducted to elucidate the difference in isomerisation pathways, if any, in solution.

Author contributions

DJH: data curation, formal analysis, investigation, methodology, project administration, resources, software, supervision, visualisation, writing – original draft, review & editing. WBN: formal analysis, investigation, methodology, software, visualisation, writing – original draft, review & editing. RTC: data curation, resources, writing – review & editing. GH: data curation, writing – review & editing. MAP: data curation, writing – review & editing. JR: data curation, resources, writing – review & editing. OJS: data curation, resources, writing – review & editing. ES: data curation, resources, writing – review & editing. JOFT: data curation, resources, writing – review & editing. TW: data curation, resources, writing – review & editing. JLW: writing – review & editing. RSM: conceptualisation, data curation, formal analysis, funding acquisition, investigation, methodology, project administration, resources, supervision, writing – original draft, review & editing.

Conflicts of interest

There are no conflicts to declare.

Data availability

Data for this article, including the experimentally measured photoelectron spectra are available at https://pure.soton.ac.uk at https://doi.org/10.5258/SOTON/D3646.

Supplementary information: Photoelectron spectrum calibration, centre of mass calculation description, case resampling bootstrap method description, S_0 and S_1 optimised geometries and frequencies, SA-CASSCF(14,12) N1–H potential energy curves, optimised conical intersection geometries, intrinsic reaction coordinate plot, nudged elastic band local minimum frequencies, and coordinates of the local minimum, transition state, and imidazole from the nudged elastic band calculations. See DOI: **https://doi.org/10.1039/d5cp02684a**

Acknowledgements

All authors would like to thank the Science and Technology Facilities Council for access to the Artemis facility. All authors acknowledge the use of the IRIDIS High Performance Computing Facility, and associated support services at the University of Southampton, in the completion of this work. DJH would like to thank ELI Beamlines and the University of Southampton for a studentship. RSM thanks the EPSRC for financial support (EP/X027635/1 and EP/R010609/1) and RSM and JLW thanks the Leverhulme trust for financial support (RPG-2021-257). RTC thanks the EPSRC for financial support (EP/X026981/1). All authors would like to thank Henry Thompson (University of Southampton), Grite Abma, and Daniel Horke (Both Radboud University) for their assistance and involvement in the first run of this experiment at Artemis in April 2023.

Notes and references

1 C. E. Crespo-Hernández, B. Cohen, P. M. Hare and B. Kohler, *Chem. Rev.*, 2004, **104**, 1977–2020.
2 C. T. Middleton, K. de La Harpe, C. Su, Y. K. Law, C. E. Crespo-Hernández and B. Kohler, *Annu. Rev. Phys. Chem.*, 2009, **60**, 217–239.
3 K. M. Hanson and J. D. Simon, *Proc. Natl. Acad. Sci. U. S. A.*, 1998, **95**, 10576–10578.
4 M. Norval, *Prog. Biophys. Mol. Biol.*, 2006, **92**, 108–118.
5 H. Yu, N. L. Evans, V. G. Stavros and S. Ullrich, *Phys. Chem. Chem. Phys.*, 2012, **14**, 6266–6272.
6 G. M. Roberts, C. A. Williams, M. J. Paterson, S. Ullrich and V. G. Stavros, *Chem. Sci.*, 2012, **3**, 1192–1199.
7 R. Crespo-Otero, M. Barbatti, H. Yu, N. L. Evans and S. Ullrich, *ChemPhysChem*, 2011, **12**, 3365–3375.
8 M. Barbatti, H. Lischka, S. Salzmann and C. M. Marian, *J. Chem. Phys.*, 2009, **130**, 034305.
9 L. Buglioni, F. Raymenants, A. Slattery, S. D. A. Zondag and T. Noël, *Chem. Rev.*, 2022, **122**, 2752–2906.
10 G. Goti, K. Manal, J. Sivaguru and L. DellAmico, *Nat. Chem.*, 2024, **16**, 684–692.
11 A. G. Griesbeck and M. Oelgemoller, *Chem. Int.*, 2023, **45**, 24–26.
12 C. Lefebvre, L. Fortier and N. Hoffmann, *Eur. J. Org. Chem.*, 2020, 1393–1404.
13 M. A. Alam, *Future Med. Chem.*, 2023, **15**, 2011–2023.
14 W. Z. R. Benson Nicole and D. Adam, *J. Visualized Exp.*, 2021, e61944.
15 M. Pokladko-Kowar, E. Gondek, A. Danel, T. Uchacz, P. Szlachcic, K. Wojtasik and P. Karasiński, *Crystals*, 2022, **12**, 434.

16 M.-D. Su, *J. Phys. Chem. A*, 2008, **112**, 10420–10428.
17 B.-B. Xie, X.-Y. Liu, Q. Fang, W.-H. Fang and G. Cui, *J. Phys. Chem. Lett.*, 2017, **8**, 1019–1024.
18 C. A. Williams, G. M. Roberts, H. Yu, N. L. Evans, S. Ullrich and V. G. Stavros, *J. Phys. Chem. A*, 2011, **116**, 2600–2609.
19 G. A. King, T. A. A. Oliver, M. G. D. Nix and M. N. R. Ashfold, *J. Chem. Phys.*, 2010, **132**, 064305.
20 A. D. Smith, E. M. Warne, D. Bellshaw, D. A. Horke, M. Tudorovskya, E. Springate, A. J. H. Jones, C. Cacho, R. T. Chapman, A. Kirrander and R. S. Minns, *Phys. Rev. Lett.*, 2018, **120**, 183003.
21 F. Frassetto, C. Cacho, C. A. Froud, I. E. Turcu, P. Villoresi, W. A. Bryan, E. Springate and L. Poletto, *Opt. Express*, 2011, **19**, 19169–19181.
22 C. Lee, W. Yang and R. G. Parr, *Phys. Rev. B: Condens. Matter Mater. Phys.*, 1988, **37**, 785–789.
23 A. D. Becke, *J. Chem. Phys.*, 1993, **98**, 5648–5652.
24 P. J. Stephens, F. J. Devlin, C. F. Chabalowski and M. J. Frisch, *J. Phys. Chem.*, 1994, **98**, 11623–11627.
25 F. Neese, *Wiley Interdiscip. Rev.: Comput. Mol. Sci.*, 2025, **15**, e70019.
26 T. Shiozaki, *Wiley Interdiscip. Rev.: Comput. Mol. Sci.*, 2018, **8**, e1331.
27 W. Humphrey, A. Dalke and K. Schulten, *J. Mol. Graphics*, 1996, **14**, 33–38.
28 I. Walker, M. Palmer, M.-J. Hubin-Franskin and J. Delwiche, *Chem. Phys. Lett.*, 2003, **367**, 517–522.
29 G. Henkelman, B. P. Uberuaga and H. Jónsson, *J. Chem. Phys.*, 2000, **113**, 9901–9904.
30 S. A. Elroby, O. I. Osman and S. G. Aziz, *Mol. Phys.*, 2011, **109**, 1785–1795.
31 J. M. Anglada, M. T. C. Martins-Costa, J. S. Francisco and M. F. Ruiz-López, *J. Am. Chem. Soc.*, 2024, **146**, 14297–14306.
32 S. K. Pal, A. S. Mereshchenko, E. V. Butaeva, P. Z. El-Khoury and A. N. Tarnovsky, *J. Chem. Phys.*, 2013, **138**, 124501.
33 C. Bannwarth, S. Ehlert and S. Grimme, *J. Chem. Theory Comput.*, 2019, **15**, 1652–1671.
34 A. Stolow, A. E. Bragg and D. M. Neumark, *Chem. Rev.*, 2004, **104**, 1719–1758.
35 S. Cradock, R. Findlay and M. Palmer, *Tetrahedron*, 1973, **29**, 2173–2181.
36 J. Rumble, *CRC Handbook of Chemistry and Physics*, CRC Press, 2020.